

# Outdoor sound propagation with analytic ray curve tracer and Gaussian beam

Qi Mo,<sup>a)</sup> Hengchin Yeh, Ming Lin, and Dinesh Manocha

*Department of Computer Science, University of North Carolina, Chapel Hill, North Carolina 27514, USA*

(Received 17 April 2015; revised 30 January 2017; accepted 7 February 2017; published online 31 March 2017)

Outdoor sound propagation benefits from algorithms that can handle, in a computationally efficient manner, inhomogeneous media, complex boundary surfaces, and large spatial expanse. One recent work by Mo, Yeh, Lin, and Manocha [Appl. Acoust. **104**, 142–151 (2016)] proposed a ray tracing method using analytic ray curves as tracing primitives, which improved the performance of propagation paths computation over rectilinear ray tracers. In this paper, an algorithm is developed that extends the performance improvement to field computation; it combines the analytic ray curve tracer with fast pressure computation based on the Gaussian beam model. The algorithm is validated against published results on benchmarks in atmospheric and ocean acoustics, and its application is demonstrated on a scene with terrains and buildings of realistic complexity and under a variety of atmospheric conditions. This algorithm is able to compute characteristic sound fields for fully general media profiles and complex three dimensional scenes at close-to-interactive speed.

© 2017 Acoustical Society of America. [<http://dx.doi.org/10.1121/1.4977005>]

[PBB]

Pages: 2289–2299

## I. INTRODUCTION

Sound propagation in outdoor environments,<sup>1–3</sup> including atmospheric and underwater acoustics, must deal with spatially varying as well as moving media. The media profiles used as input to sound propagation can come from empirical models, real-world measurements, or from computational flow simulation. Obstacles' shape and material properties play an important role as well, especially for scenes with complex terrains or area with dense man-made structures. As data that describe the media conditions and the scene obstacles become increasingly available with ever richer details, methods for outdoor sound propagation needs to be able to account for the full scale of those data.

Existing methods face many challenges in handling such complexity; they either make assumptions that preclude a fully general medium or complex obstacles in the scene, or they become prohibitively expensive with large, general scenes. Models such as fast field program (FFP), parabolic equation (PE), and normal modes fall in the former category, while methods like finite difference time domain (FDTD), finite elements method (FEM), and boundary element method (BEM) belong to the latter.

Geometric acoustics (GA)<sup>4</sup> methods like ray models are known for their efficiency in handling boundary surfaces under the assumption of homogeneous media and rectilinear paths. Recent works<sup>5,6</sup> has also attempted to accommodate inhomogeneous media by tracing parabolic ray curves as primitives, which significantly accelerates path computation. On the other hand, ray models suffer from artifacts in caustics and shadow zones when computing fields; while models such as the Gaussian beam<sup>7</sup> perform better in this regard. However, the performance of Gaussian beam can be

hindered by the underlying numerical path integration, which remains slow for inhomogeneous media.

We combine the performance of the analytic ray curve tracer<sup>6</sup> and the accuracy of the Gaussian beam<sup>7</sup> into an algorithm for outdoor sound propagation. In particular:

- (1) We compute analytic solutions to on-ray pressure as well as near-ray fields based on the parabolic ray formulation (Sec. III), which leads to efficient field computation that matches the efficiency of the path computation.
- (2) We combine the Gaussian beam model with the analytic ray tracer and validate the approach on two dimensional (2D) benchmarks<sup>8,9</sup> that are widely used in atmospheric and ocean acoustics. Our algorithm is able to replicate the published reference results generated by alternative techniques (Sec. IV).
- (3) We apply the algorithm on a three dimensional (3D) scene consisting of thousands of surface primitives modeling terrains and buildings for a set of different atmospheric conditions, which demonstrates its efficiency in computing characteristic sound fields (Sec. V).

Overall, we provide a validated solution to outdoor sound propagation that augments a fast analytic ray tracer with equally fast analytic field computations. This algorithm takes general media and scene input and computes the full 3D sound field at close-to-interactive speed, making it useful for a wide range of outdoor sound applications (Sec. VI).

## II. PRIOR WORK

Outdoor sound propagation has been studied extensively in underwater<sup>3</sup> and atmospheric acoustics.<sup>1</sup> Here we first review numerical methods that provide full wave solutions, including hybrid schemes aiming at reducing the high

<sup>a)</sup>Electronic mail: qmo@cs.unc.edu

computation cost of wave-based methods. Next, we review ray-based methods and their advantages and limitations for outdoor scenarios.

### A. Wave-based methods

Early methods, including FFP and PE, provide frequency-domain, full-wave solutions that account for the inhomogeneous media, but depend upon simplifying assumptions about the media and scene configurations. In scenarios that meet those assumptions, these models have been thoroughly validated<sup>10–13</sup> and often serve as reference solutions to test other models.

Among the general numerical methods that handle arbitrary media and obstacles, one widely used method is the FDTD method, which solves the linearized Euler equation.<sup>14,15</sup> FDTD has been coupled with flow simulation;<sup>16,17</sup> it has been applied with various ground conditions,<sup>18</sup> terrains,<sup>19–21</sup> and complex obstacles.<sup>22–24</sup> As a time-domain method, it is also used for pulse propagation.<sup>23,25</sup> The main disadvantage of FDTD is its limited scalability with domain volume or frequency; this limitation makes it prohibitively expensive for large-scale broadband simulation, and limits its usefulness for wide area to low-frequency cases.<sup>26</sup> Methods such as pseudo spectral time domain (PSTD)<sup>27,28</sup> and transmission line matrix (TLM)<sup>29–31</sup> are more efficient, but they are still fundamentally limited by the cost of discretizing a large domain.

To address the scalability problem, many hybrid methods have been developed. Some use FDTD in confined areas and apply PE to propagation over long range and relatively sparse space.<sup>32–34</sup> Others, such as BEM or the equivalent source method (ESM), were employed to limit the computation either to boundary surfaces or to volumes that bound scatterers tightly. But these methods introduced new issues. BEM, which must be coupled with specialized Green function for refractive media, scales poorly with surface area and frequency. ESM, when coupled with ray models<sup>35</sup> to handle large domains, does not scale well with the number or complexity of scatterer objects. A more recent method, adaptive rectangular decomposition (ARD),<sup>36,37</sup> took advantage of the analytic solution of the wave equation in a rectangular domain, but it requires constant sound speed within each spatial subdivision, which is not easily adapted to a general medium profile.

### B. Geometric acoustics methods

GA methods<sup>4</sup> are widely used in room acoustics<sup>38</sup> to handle high-order surface interactions under the assumption of a homogeneous medium. Examples include the image source method,<sup>39,40</sup> ray tracing,<sup>41,42</sup> beam tracing,<sup>43</sup> and path tracing.<sup>44</sup>

Ray models have also been applied to inhomogeneous media<sup>3</sup> by numerically integrating the ray equations. While a sparse set of rays can be efficiently traced to plot out the propagation paths, long-range propagation and pressure field computation that requires dense rays become expensive. When the ray models are used to compute the pressure field, they are known to have issues in the caustic zones and in the

shadow zones. The Gaussian beam approach,<sup>7</sup> which was developed in seismology and applied on underwater<sup>45</sup> and atmospheric<sup>46</sup> acoustics, improves the accuracy in caustics and shadow zones. However, when the underlying paths are still computed by numerical ray integration, the performance is limited by the integration step sizes. One recent work<sup>6</sup> achieved significant performance improvement by replacing the numerical ray integration with segments of parabolic ray curves. We give an overview of this ray tracer in the next section, and then introduce our algorithm, which combines this ray tracer with the Gaussian beam.

## III. ALGORITHM

An overview of our algorithm is illustrated in Fig. 1. Our algorithm is built upon an efficient ray tracer that outputs propagation paths made up of segments of analytic curves (Sec. III A). We compute a set of additional variables for each ray segment by analytic evaluations of constant cost, which extends the path-computation efficiency to pressure computation. These variables are subsequently used for computing pressure both on the ray paths (Sec. III B) and in the near-ray regions (Sec. III C). Here we adopt the term *ray paraxial* defined by Červený<sup>7</sup> to refer to the near-ray regions, and we use a paraxial Gaussian beam model to approximate the field near a central ray. The mathematical derivation that leads to this algorithm is a special case of the more general ray theory discussed in depth in Červený's comprehensive work;<sup>7</sup> details can be found in [Appendixes A–F](#) to this paper.

### A. Analytic ray curve tracer

Given a medium profile with a spatially varying sound speed  $V(\vec{x})$ , we assume a locally constant gradient of  $V^{-2}$ :  $V(\vec{x})^{-2} = A_0 + \vec{A} \cdot \vec{x}$  within a certain range around  $\vec{x}$ . The trajectory of ray originating from  $\vec{x}$  with initial direction  $\vec{t}_0$  can be shown to be a parabolic curve that lies in the plane with the normal of  $\vec{A} \times \vec{t}_0$  [the *ray plane*, see Fig. 2(a)]. The intersection between the parabolic ray curve and any planar surface can be solved analytically, and key properties such as position  $\vec{x}$ , tangent direction  $\vec{t}$ , the travel time  $T$ , and the *slowness vector*  $\vec{p} = \nabla T$  (the direction of which coincides  $\vec{t}$ ) can be computed for any point along the ray by analytic evaluations of constant cost ([Appendix A](#)).

This analytic ray formulation enables a ray tracer that computes propagation paths in a general medium consisting of consecutive segments of parabolic curves. In smooth media, the assumption of constant  $\nabla V^{-2}$  generally holds for a range larger than the assumption of constant  $V$ , enabling the ray curve tracer to advance in longer segments than rectilinear ray tracer; this is one of the key sources of performance improvement. Adaptive segment sizes based on on-the-fly media sampling, as well as acceleration structure that bounds surfaces and ray curves, lead to further speedup that amounts to one to two orders of magnitude improvements over numerical ray integration on 3D scenes.<sup>6</sup>

The ray curve tracer uses the heuristic that the range of validity  $d(\vec{x})$  for a local  $\nabla V^{-2}$  should be proportional to  $\|\nabla V^{-2}\|$ , so that the constant gradient assumption remains valid for a relatively small spatial range in areas of great

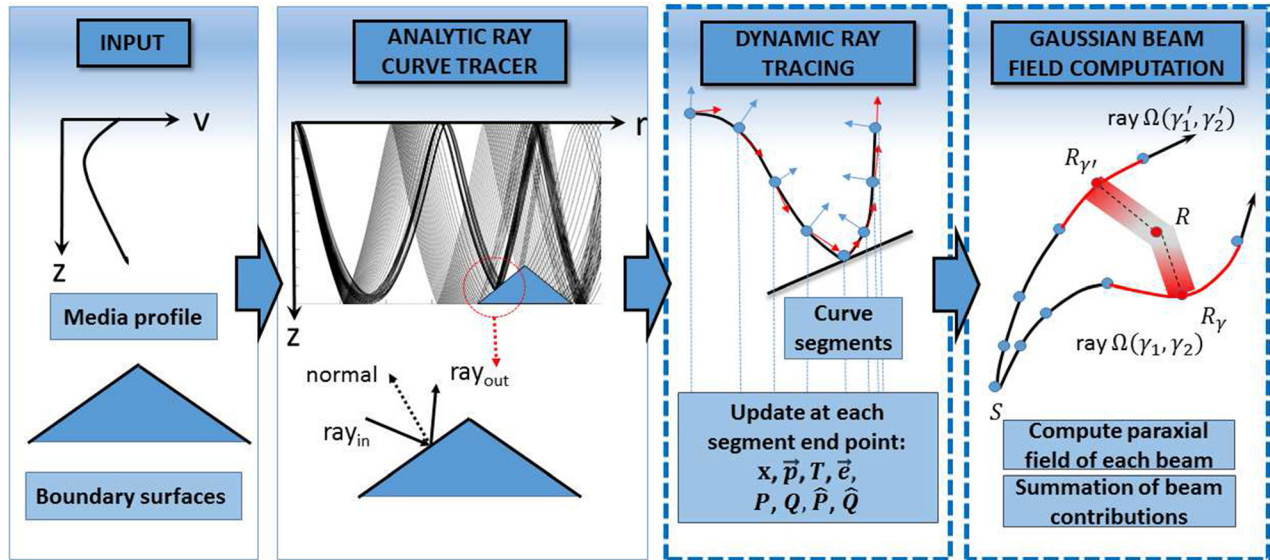


FIG. 1. (Color online) Algorithm overview. Given an input media profile and boundary surfaces, the analytic ray tracer (Ref. 6) output propagation paths made up of segments of parabolic curves (reviewed in Sec. III A). Our algorithm (the two boxes on the right) then perform dynamic ray tracing that evaluates a set of derivatives analytically and efficiently for pressure along the path (Sec. III B), and the pressure for field point  $R$  is computed by summing paraxial contributions from each path based on the Gaussian beam model (Sec. III C).

media variation. Controlled by a global parameter  $\delta$ , we compute  $d(\vec{x})$  from  $\delta = \frac{1}{8} \|\nabla V^{-2}\| d^3(\vec{x})$ . The on-the-fly medium-gradient sampling also enables us to handle vector wind field by adding the wind speed  $\vec{w}(\vec{x})$  projected onto the ray direction  $\vec{t}$ :  $V(\vec{x}) + \vec{w}(\vec{x}) \cdot \vec{t}(\vec{x})$ .

## B. Dynamic ray tracing

Dynamic ray tracing, as defined by Červený,<sup>7</sup> keeps track of how a set of derivatives in ray-centered coordinates progress among propagating rays; the derivatives are subsequently used to compute pressure and travel time along the ray. We perform dynamic ray tracing analytically for each segment of parabolic ray curve, which achieves efficiency in pressure computation that matches the efficiency of the analytic ray tracer.

First we define the coordinates involved. The *ray-centered coordinates*  $q_1, q_2, q_3$  are defined for any point along a particular ray  $\Omega$  with origin at that point. The  $q_3$ -axis follows  $\Omega$ ; the  $q_1$ -axis and  $q_2$ -axis are taken to be perpendicular to

the  $q_3$ -axis as well as being perpendicular to one another. Transformation from the ray-centered coordinates  $q_k$  to Cartesian coordinates  $x_i$  is accomplished by the  $3 \times 3$  matrix  $\hat{H}$ ,  $\hat{H}_{ik} = \partial x_i / \partial q_k$ ,  $i, k = 1, 2, 3$ , and  $\hat{H}^{-1} = \hat{H}^T$  transforms Cartesian coordinates back to ray-centered coordinates.

The derivatives we seek in dynamic ray tracing capture the changes in spatial relationships among rays traveling through a medium profile. Consider a system of rays starting from a source and parameterized by *ray parameters*  $\gamma_1, \gamma_2$ , taken here as the azimuth  $\phi_0$  and elevation  $i_0$  angles. The  $2 \times 2$  matrices  $\mathbf{Q}$  and  $\mathbf{P}$  are defined with elements  $Q_{IJ} = (\partial q_I / \partial \gamma_J)_{T=\text{const}}$ ,  $P_{IJ} = (\partial p_I^{(q)} / \partial \gamma_J)_{T=\text{const}}$ ,  $I, J = 1, 2$ , which are derivatives of the ray-centered coordinates and the slowness vector in the ray-centered coordinates with respect to the ray parameters. Correspondingly,  $\hat{\mathbf{Q}}^{(x)}$  and  $\hat{\mathbf{P}}^{(x)}$  are defined with elements  $Q_{ij}^{(x)} = (\partial x_i / \partial \gamma_j)_{T=\text{const}}$ ,  $P_{ij}^{(x)} = (\partial p_i^{(x)} / \partial \gamma_j)_{T=\text{const}}$ , in Cartesian coordinates,  $\hat{\mathbf{H}}^{(x)}$  is defined with elements  $H_{ij}^{(x)} = \hat{H}_{ij}$ ,  $i = 1, 2, 3$ ,  $J = 1, 2$ , and

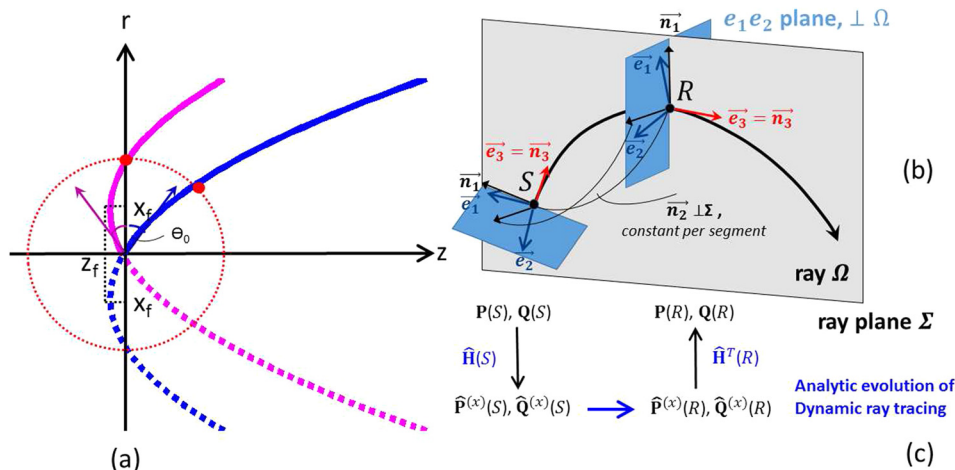


FIG. 2. (Color online) (a) Analytic ray curve segment in the ray-plane. Rays of two different initial directions  $\vec{t}_0$  are drawn.  $(x_f, z_f)$  is the vertex of the parabola. We assume a locally constant  $\nabla V^{-2}$ , the assumption's range of validity (dotted circle) determines the extent of the ray segment (Sec. III A). (b), (c) Analytic dynamic ray tracing: analytic evolution of  $\mathbf{P}, \mathbf{Q}$  are performed for each segment by transforming into and evolving in Cartesian coordinates before transforming back to ray-centered coordinates (Sec. III B). The unit basis  $\vec{e}_1, \vec{e}_2, \vec{e}_3$  and  $\vec{n}_1, \vec{n}_2, \vec{n}_3$  are defined in Appendix C.

$\hat{\mathbf{Q}}^{(x)} = \hat{\mathbf{H}}\mathbf{Q}$ ,  $\hat{\mathbf{P}}^{(x)} = \hat{\mathbf{H}}\mathbf{P}$ . Along a parabolic ray curve,  $\hat{\mathbf{Q}}^{(x)}$  and  $\hat{\mathbf{P}}^{(x)}$  can be evolved analytically (Appendix B), and  $\hat{\mathbf{H}}^{(x)}$  can also be evolved analytically (Appendix C); we thereby achieve analytic evolution of  $\mathbf{P}$  and  $\mathbf{Q}$  (Appendix D) [see Figs. 2(b) and 2(c)].

The pressure amplitude  $P^{\text{ray}}$  at any point  $s$  along the ray given  $P(s_0)$  at source  $s_0$  is

$$P^{\text{ray}}(s) = \left[ \frac{\rho(s)V(s)J(s_0)}{\rho(s_0)V(s_0)J(s)} \right]^{1/2} P(s_0), \quad (1)$$

where  $\rho$  is the density of the medium, and  $J = \det \mathbf{Q}$  is the ray Jacobian [Červený, Eq. (3.10.53)].  $\mathbf{P}$  and  $\mathbf{Q}$  are also used in computing the paraxial field, as explained in Sec. III C.

### C. Field computation with Gaussian beam

We use Gaussian beam model to approximate paraxial fields in the vicinity of ray paths; this involves computing paraxial travel time and paraxial pressure amplitude, both of which benefit from the efficient dynamic ray tracing described in Sec. III B above. As shown in the rightmost block of Fig. 1, we gather all segments of ray curves that pass in the vicinity of a given field point, compute the paraxial pressure amplitude and travel time from each segment, and sum up the contribution (Appendix F). For a field of large volume, we save the costs of locating vicinity ray segments for each field point

by reversing the process, distributing the pressure contribution from each beam to the field points it covers.

Based on the definition of  $\mathbf{P}$  and  $\mathbf{Q}$ , we introduce the  $2 \times 2$  matrix:

$$\mathbf{M} = \mathbf{P}\mathbf{Q}^{-1}, \quad M_{IJ} = (\partial p_I^{(q)} / \partial q_J)_{T=\text{const}}, \quad I, J = 1, 2. \quad (2)$$

Recall that the slowness vector  $\vec{p}$  is the first derivative of  $T$ ;  $\mathbf{M}$  is, therefore, the second derivative of  $T$  with respect to ray-centered coordinates. For a point  $R'$  in the vicinity of a ray  $\Omega$ , the paraxial travel time at  $R'$  can be computed given the  $T$  at a point  $R$  on  $\Omega$ :

$$T(R', R) = T(R) + \frac{1}{2} \mathbf{q}^T(R') \mathbf{M}(R) \mathbf{q}(R'), \quad \mathbf{q} = (q_1, q_2)^T, \quad (3)$$

when  $\Omega^\perp$  is the plane perpendicular to  $\Omega$  that passes  $R'$ , and point  $R$  is the intersection of the ray  $\Omega$  and  $\Omega^\perp$ . The derivatives of  $T$  can also be approximated in Cartesian coordinates, in which case any point  $R_\gamma$  on the ray that is close to  $R'$  can be selected, saving the costs of computing  $\Omega^\perp$  and  $R$  (Appendix E).

The Gaussian beam model computes a paraxial amplitude centered on the ray with a Gaussian drop-off, which is achieved by allowing the matrix  $\mathbf{M}$  to be complex:  $\mathbf{M} = \text{Re}(\mathbf{M}) + i\text{Im}(\mathbf{M})$ .  $\text{Im}(\mathbf{M})$  is chosen to be positive definite as described in Ref. 7, so that

$$p^{\text{beam}}(R') = P^{\text{ray}}(R) \exp \left[ -i\omega \left( -T(R) - \frac{1}{2} \mathbf{q}^T(R') \text{Re}(\mathbf{M}(R)) \mathbf{q}(R') \right) \right] \exp \left[ -\frac{1}{2} \omega \mathbf{q}^T(R') \text{Im}(\mathbf{M}(R)) \mathbf{q}(R') \right]. \quad (4)$$

## IV. VALIDATION

We validated our algorithm on two benchmark scenes of atmospheric and oceanic sound propagation. The first benchmark was proposed<sup>8</sup> with reference results generated by a few different methods that agree with each other, and has since been widely adopted by other atmospheric acoustics works for validation purposes. The second benchmark comes from ocean acoustics, with the representative Munk profile and a conical seamount as bathymetry. Results have been reported for the Munk profile in many works, and one of the latest works<sup>9</sup> contains reference results generated by normal modes. We compute 2D pressure fields for these benchmarks and compare the results directly with published results in the literature. Although the ray-based method is a high-frequency approximation, we achieve good agreement with the reference results, and we were able to replicate the characteristic interference patterns for frequency as low as 10 Hz. After establishing the validity of our method with these benchmarks, we demonstrate the application of our method to a realistic 3D scene with more complex media

conditions in Sec. V. For all benchmarks, we compute the sound field in terms of the transmission loss (TL), which is defined as  $\text{TL}(\vec{x}) = 20 \log |p(\vec{x})/p_0(r = 1 \text{ m})|$ , where  $|p_0(r)| = 1/4\pi r$  is the pressure modulus at a distance  $r$  from the source in free space.

### A. Benchmark A (inhomogeneous atmosphere, flat ground with impedance)

In Attenborough *et al.*,<sup>8</sup> a set of benchmark cases for outdoor sound propagation is proposed, and results generated by a range of methods show good agreements, including FFP, PE, normal modes, ray and beam tracing. The boundary surface in the scene is a flat ground with impedance, while the media is inhomogeneous with three different profiles.

#### 1. Media profile

Sound speed  $V(x)$  at spatial location  $x$  with height  $z(x)$  is given by

Case 1: Downward refractive  $V(x) = 343 + 0.1z(x)$  (m/s);

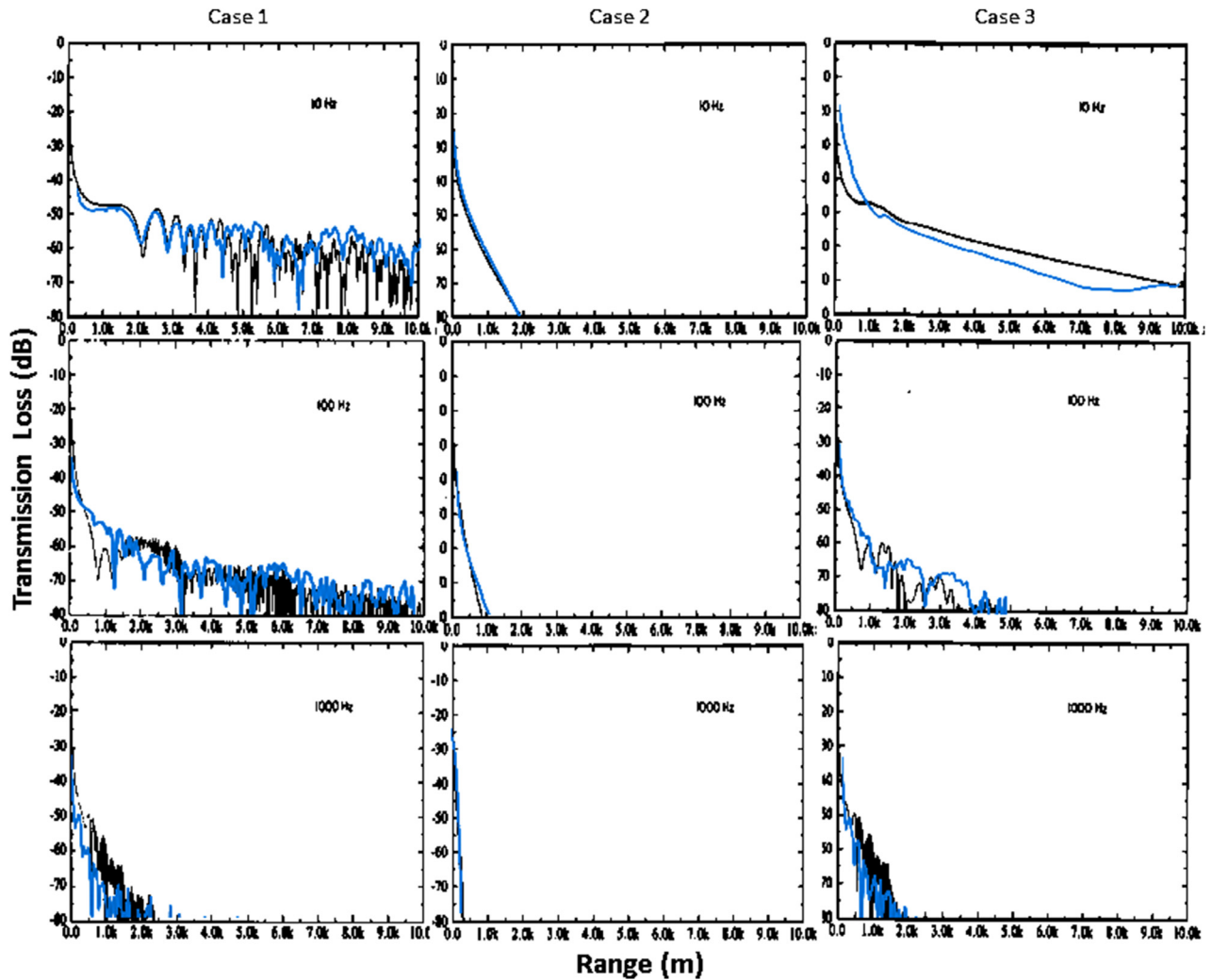


FIG. 3. (Color online) Benchmark A Range-TL plot: Source height  $h_s = 5$  m, receiver height  $h_r = 1$  m, range 10 km. Columns contain results for media profiles case 1, 2, and 3, while rows contain results for frequency 10, 100, and 1000 Hz. The results computed by our algorithm are plotted on top of the reference results from Figs. 12–14 (Ref. 8).

Case 2: Upward refractive  $V(x) = 343 - 0.1z(x)$  (m/s);

Case 3: Combine case 1 and 2 with  $V(z=0) = 343$  (m/s),  $\delta V = 0.1$  for  $z(x) < 100$  m,  $\delta V = -0.1$  for  $100 \text{ m} < z(x) < 300$  m, and constant  $V$  for  $z(x) > 300$  m.

## 2. Ground impedance

A four parameter model is used to compute the impedance of the flat ground, and the same parameters from Attenborough

*et al.*<sup>8</sup> are used. Results: As shown in Figs. 3 and 4, our algorithm is able to replicate the interference pattern for this set of media conditions at three different frequencies. 1D range plot and 2D vertical field of resulting TL is included for direct comparison with figures in Ref. 8. In particular, the side-by-side comparison of 1D range plot in Fig. 3 shows that our results match the reference results across all three conditions and all three frequencies. Previous work based on Gaussian beams was reported to have difficulties with upward refractive conditions

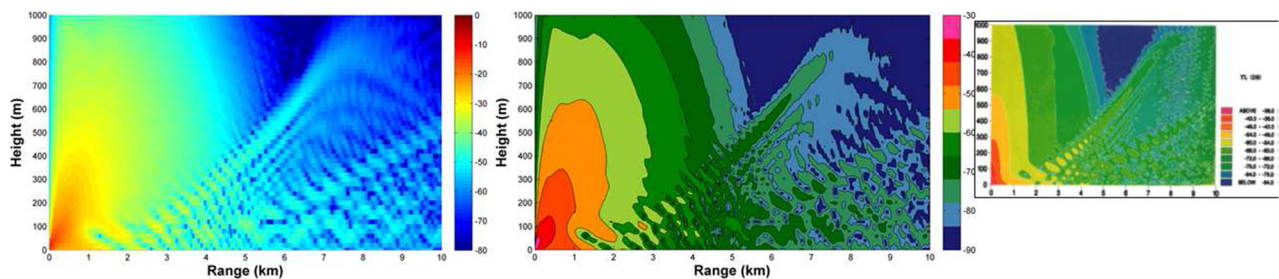


FIG. 4. (Color online) Benchmark A 2D Field: Source height  $h_s = 5$  m, receiver height  $h_r = 1$  m, frequency 10 Hz. 2D vertical field of height up to 1 km and range up to 10 km is visualized on the left, and the corresponding contour plot is shown on the right for comparison with Fig. 15 (Ref. 8).

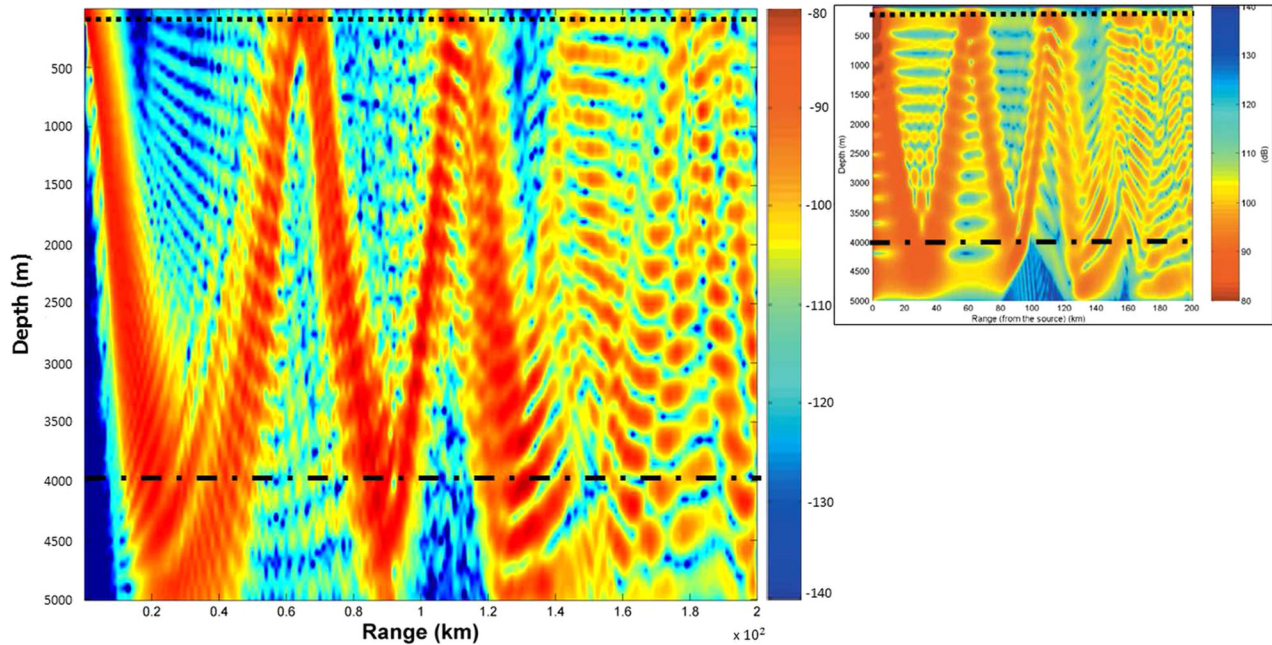


FIG. 5. (Color online) Benchmark B 2D field: Source depth 100 m, frequency 10 Hz. 2D vertical field of TL is visualized for depth up to 5 km and range up to 200 km, compared to Fig. 9 (Ref. 9).

at ranges over 200 m,<sup>46</sup> but our method achieves high accuracy for such condition (case 2) over a range of 10 km. This is potentially because that the previous method limited the beam width to avoid truncation of reflected beams, which in turn caused the beams reaching the receiver to be overly narrow. Our method does not rely on explicit construction of beams (we compute the listener's location within a beam by directly computing the geometric relationships between the listener and the central ray of the beam), and therefore does not need to clip the beams against reflection surfaces nor to limit the beam width. For this benchmark our ray method produces results of accuracy approaching wave-based methods, which have not been achieved by existing ray-based methods. Furthermore, the number of rays required for this benchmark is as low as 21 rays for the reported results, more rays can be traced to compute more accurate pressure fields.

## B. Benchmark B (Munk profile with conical seamount)

We validate our algorithm on an underwater benchmark with the standard Munk profile and a conical seamount as bathymetry. The Munk profile is an idealized profile that describes the sound speed variation for depth up to 5000 m. This benchmark spans a much larger range and depth than the atmospheric benchmark above, has a non-linear sound speed variation, and contains a seamount obstacle in the scene. Published results for this benchmark, computed by normal modes, can be found in prior work.<sup>9</sup>

### 1. Media profile

$$V(z) = 1500[1 + \epsilon(\tilde{z} - 1 + e^{-\tilde{z}})], \quad \epsilon = 0.00737,$$

$$\tilde{z} = \frac{2(z - 1300)}{1300}.$$

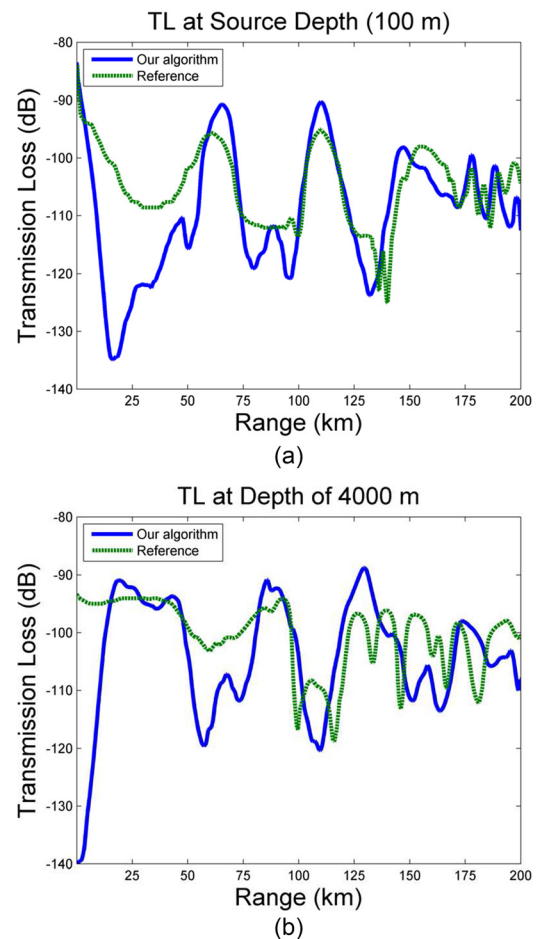


FIG. 6. (Color online) Benchmark B 1D plot: Source depth 100 m, frequency 10 Hz. 1D TLs are plotted for the source depth (100 m) and the depth of 4000 m (clearing the top of the conical seamount). See dashed lines in Fig. 5 for the corresponding depths plotted here. Reference plots are generated from Fig. 9 (Ref. 9).

## 2. Bathymetry

Conical seamount: range 100 km, height 1000 m, radius of base 20 km.

## 3. Bottom impedance

Fluid half space with compressional speed of 2000 m/s, density of  $1 \text{ g/cm}^3$ , and attenuation of  $0.1 \text{ dB}/\lambda$ .

## 4. Results

The vertical 2D field is visualized in Fig. 5, and 1D fields at two sample depths are plotted in Fig. 6. For this underwater benchmark with extensive volume, our ray tracer successfully replicated the characteristics of the field by tracing 200 rays with launch angles uniformly distributed within  $\pi/6$  of the horizontal direction, focusing on the long-range propagating paths. Results are compared with the published results computed by normal modes available in prior work.<sup>9</sup> The biggest discrepancy happens in the range of 0–20 km, potentially due to the limited ray launch angles.

## V. APPLICATION ON COMPLEX OUTDOOR SCENE

### A. Scene configuration

#### 1. Media

We generate a general medium profile based on a commonly used empirical model of the atmosphere.<sup>1</sup> The acoustic index of refraction in the atmosphere ( $n = V_0/V$ , where  $V_0$  is the reference sound speed) is modeled with a stratified component  $n_{\text{str}}$  and a fluctuation component  $n_{\text{flu}}$ , so that

$n = n_{\text{str}} + n_{\text{flu}}$ . The stratified component follows a logarithmic profile of the altitude  $z$ :  $n_{\text{str}}(z) = V_0 / \{V_0 + b \ln[(z/z_g) + 1]\}$ , where  $z_g = 1 \text{ m}$  is the roughness length of the ground surface, and a typical value for  $b$  is 1 m/s for a downward-refracting atmosphere and  $-1 \text{ m/s}$  for an upward-refracting atmosphere. The fluctuation component at position  $\vec{x}$  can be computed as  $n_{\text{flu}}(\vec{x}) = \sum_i G(\vec{k}_i) \cos(\vec{k}_i \cdot \vec{x} + \alpha_i)$ , where  $\vec{k}_i = (k_i \cos \phi_i \sin \theta_i, k_i \sin \phi_i \sin \theta_i, k_i \cos \theta_i)$  is the wave vector describing the spatial frequency of the fluctuation, and  $k_i = i\Delta k$  for  $i = 1, 2, \dots, N$ .  $\phi_i$  and  $\alpha_i$  are random angles between 0 and  $2\pi$ ,  $\theta_i$  is a random angle chosen so that  $\cos \theta_i$  are distributed uniformly between 1 and  $-1$ .  $G(\vec{k}_i)$  is a normalization factor computed using the Gaussian spectrum with the correlation length  $a = 1.0 \text{ m}$  and the standard deviation  $\mu_0$  of the refractive index  $\mu$  to be  $\mu_0^2 = 1 \times 10^{-5}$ . This model represents simplified conditions assuming isotropic atmosphere and fixed correlation length of turbulence. Profiles generated by more complex models can be substituted as input to our algorithm.

### 2. Scene objects

We use a computer-modeled 3D scene consisting of undulating terrains with a reservoir and buildings. A wireframe rendering of the scene, with the two sound-source locations marked by dots, can be found in Fig. 7(a). The scene has a physical dimension of  $220 \text{ m} \times 150 \text{ m} \times 50 \text{ m}$ , and is represented by 4000 triangular surface primitives. Our algorithm can simulate propagation for any scenes that can be modeled or scanned into surface representations similar to the one demonstrated here.

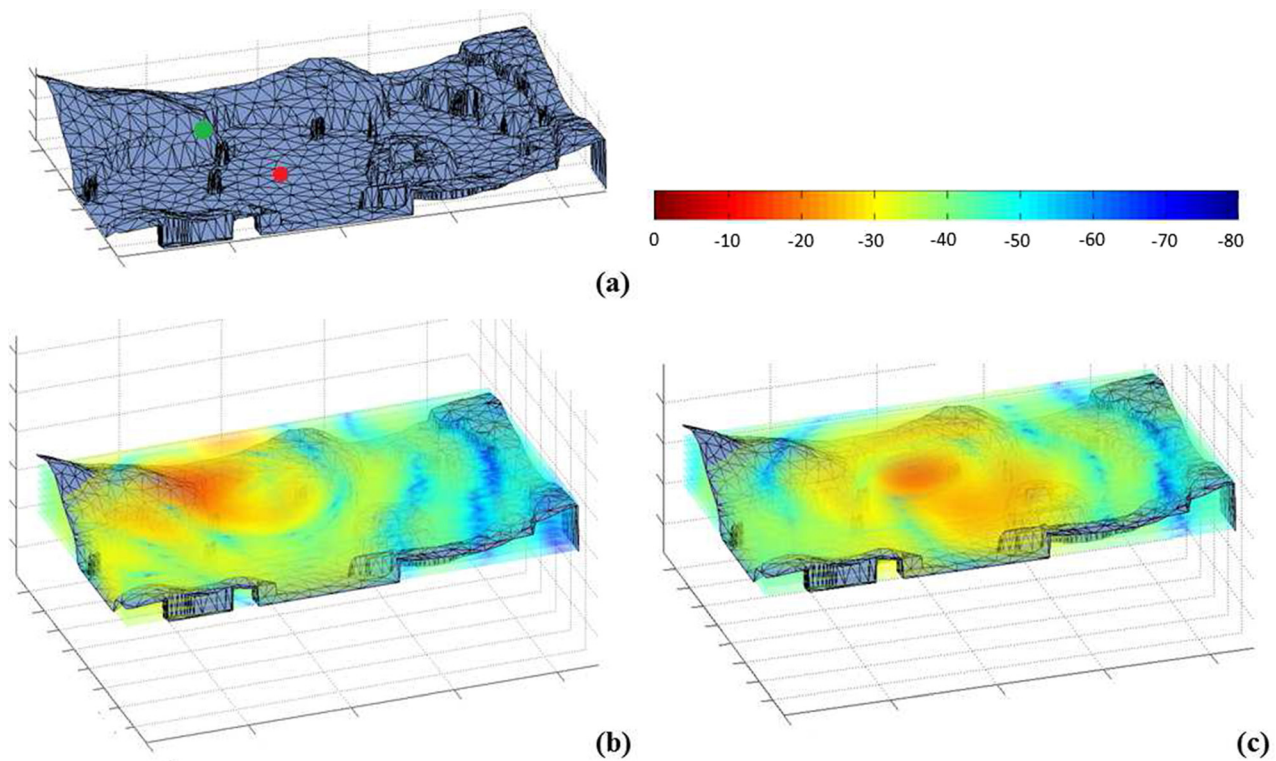


FIG. 7. (Color online) Outdoor scene and field results for two source locations: (a) Wireframe rendering of the Reservoir scene. One of the dots represents a sound source located on the slope, and the other dot represents a sound source in the valley. (b) Slices of sound TL field visualized for the source on slope. (c) Slices of sound TL level visualized for the source in the valley. Frequency 10 Hz.

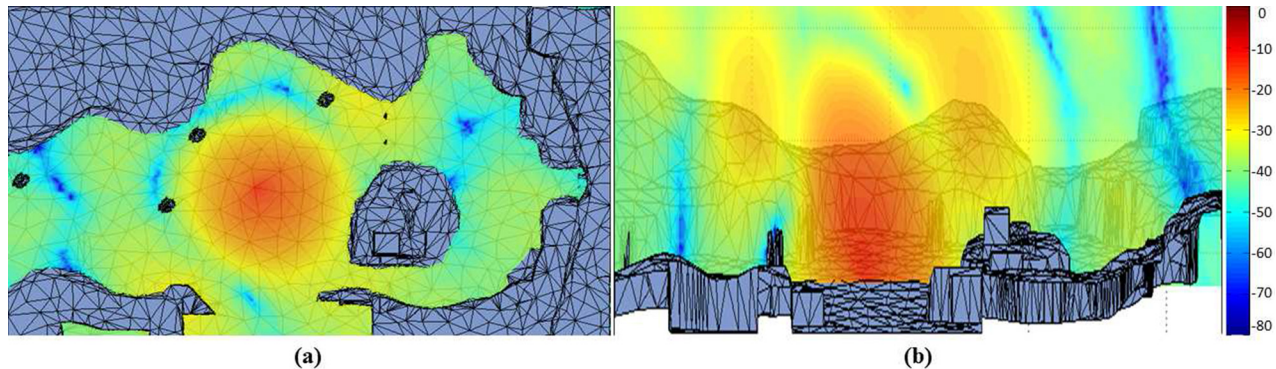


FIG. 8. (Color online) Source in the valley: Downward-refractive media. (a) Horizontal slice and (b) vertical slice, both of which pass the source location. Frequency 10 Hz.

## B. Results

We compute sound fields for two source locations [Fig. 7(a)], one on the slope of the reservoir, the other in the center of the valley. For this scene, the sound field displays characteristics resulting from the interaction of sound waves with the medium itself and with obstacles in the scene. We show a stack of slices in Fig. 7 for visualization purposes, while the full 3D field is computed by our algorithm. A source frequency of 10 Hz is used for all the visualized results in order to keep the field pattern easy to interpret. Our algorithm generate the sound fields at close to interactive rates (679 ms/frame tracing 1K initial rays for the  $220 \times 150 \times 50$  field points). At this rate, insights about field characteristics can be gained by varying the scene configurations and observe the field changes. Details on performance of our method can be found by referring to Ref. 6. It should be noted that ray tracing methods are typically used when the wavelengths are much smaller than the sizes of media inhomogeneities, which do not hold for this test scene at 10 Hz.

The diurnal changes in the atmosphere typically lead to an upward refractive condition during the day, and a downward refractive condition at night. We generate the sound

field for the source on the slope of the reservoir, and a source in the center of the valley, for upward and downward refractive conditions, respectively, and visualize the difference [Fig. 8 and Figs. 9(a) and 9(b)]. We can see that relative to upward refractive condition, the downward refractive condition leads to increased sound pressure level at several ring-shaped regions at different distances from the source, which correspond to the locations where the sound wave is bent downward, hits the ground, and then is reflected back up. Wind plays an important role in atmospheric sound propagation, creating extra variations in the sound speed profile, and interacts with physical obstacles that further complicate the sound field. For the sound source on the slope, we also simulate the sound field for up-wind and down-wind conditions [Figs. 9(c) and 9(d)], which yields similar patterns as the relative difference between upward and downward refractive media.

Our ray tracer accounts for vector wind field by dynamically sampling the medium profile during ray traversal (see Ref. 6). We show this capability with the sound source in the valley, and visualization of the difference in sound field between a north and a south wind, and between a west and an east wind, respectively (Fig. 10). The wind fields are generated to follow vertically logarithmic profiles with wind

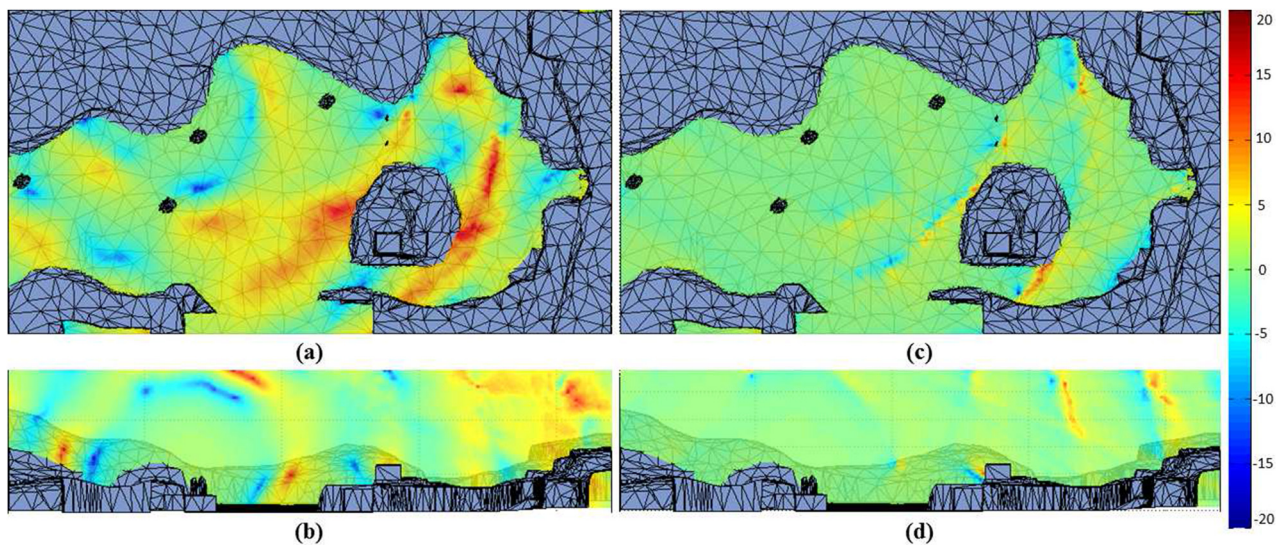


FIG. 9. (Color online) Relative sound pressure level for source on the slope. Upward vs downward refraction: (a) top view of a horizontal slice of the field; (b) front view of a vertical slice of the same field as (a). Up wind vs down wind: (c) top view of a horizontal slice of the field; (d) front view of a vertical slice of the same field as (c). Frequency 10 Hz.

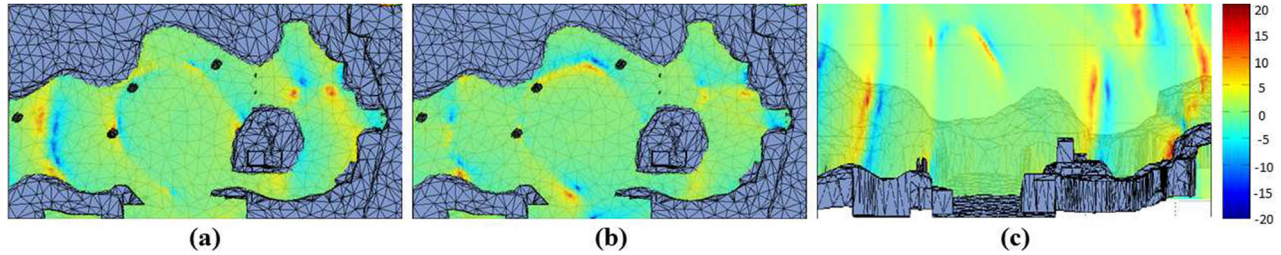


FIG. 10. (Color online) Vector wind for source in the valley: (a) Difference in horizontal field of sound pressure level between a north and a south wind. (b) Difference in horizontal field of sound pressure level between an east and a west wind. (c) Difference in vertical field of sound pressure level between an east and a west wind. Frequency 10 Hz.

speed  $w(z) = 1.826 \ln(z) + 4.16$  in the four directions, respectively, so that the expected differences in propagated fields among them are easy to interpret. The pressure difference is most prominent in the form of crescent-shaped ridges along the north-south axis (vertical in the image) and the west-east axis (horizontal in the image), respectively.

## VI. DISCUSSIONS

This algorithm is complementary to many existing sound propagation techniques and can be extended or combined in multiple ways. With the analytic ray curve tracer<sup>6</sup> as a component, our method inherits its many potential extensions, such as: augmenting GA methods with capability to handle inhomogeneous media; forming hybrid method with ESM based on frequency and spatial subdivision (similar to Yeh *et al.*<sup>35</sup>); using the ray tracer for wide area assessment that guides the application of numerical methods only in areas of interest. As in other ray models, extensions<sup>47,48</sup> to our method can also be built to account for dynamic turbulence fields. It is also possible to accommodate sound sources other than a point source, such as complex sources or sources with directivity;<sup>49,50</sup> this can be achieved by using the techniques of Gaussian beam expansion.

As a ray-based model, this algorithm inherits the limitations that it is a high-frequency approximation, not a full-wave solution. The analytic ray tracer relies on spatial coherence in the medium to perform efficiently. The Gaussian beam model that is used to compute the sound field relies on carefully chosen parameters that control the beam width,<sup>45</sup> and it is best determined on a per-scene basis.

## VII. CONCLUSION

This paper combines an analytic ray curve tracer<sup>6</sup> and the Gaussian beam model to form an efficient solution for outdoor sound field computation. Based on the parabolic ray formulation,<sup>6</sup> we use analytic solutions to compute on-ray pressure and paraxial fields in combination with a Gaussian beam model. The analytic ray tracer's path-computation efficiency is matched by our pressure-computation efficiency, and the combined algorithm can simulate the propagated sound field for large 3D outdoor scenes with general input media and complex obstacles. This algorithm is validated on 2D benchmarks with inhomogeneous media profiles that are widely used in atmospheric and underwater propagation. The results computed by our algorithm are verified against published results, generated by validated methods including

FDTD, PE, and normal modes. The capability of this algorithm is further demonstrated with a complex 3D scene under a variety of media conditions that would present scalability challenges to existing methods. Results that reflect the characteristics of the scene and media are generated at close-to-interactive speed. As future work we hope to obtain measured data or to run large scale numerical simulation to further validate and gauge the speedup of the algorithm, and to apply this algorithm on more challenging outdoor scenarios, including fully dynamic scenes.

## ACKNOWLEDGMENTS

This work was sponsored by ARO Grants No. W911NF-13-C-0037 and No. W911NF-14-1-0437, and the National Science Foundation Grant No. 1320644.

## APPENDIX A: ANALYTIC EVOLUTION OF RAY TRAJECTORIES

With ray parameter  $\sigma$  defined by  $d\sigma = V^2 dT = V ds$ , the ray trajectories  $x_i$ , slowness  $p_i$ , and travel time  $T$  can be evolved analytically from  $\sigma_0$  to any  $\sigma$  along the ray:

$$x_i(\sigma) = x_{i0} + p_{i0}(\sigma - \sigma_0) + \frac{1}{4}A_i(\sigma - \sigma_0)^2, \quad (\text{A1})$$

$$p_i(\sigma) = p_{i0} + \frac{1}{2}A_i(\sigma - \sigma_0), \quad (\text{A2})$$

$$T(\sigma) = T(\sigma_0) + V_0^{-2}(\sigma - \sigma_0) + \frac{1}{2}A_i p_{i0}(\sigma - \sigma_0)^2 + \frac{1}{12}A_i A_i(\sigma - \sigma_0)^3. \quad (\text{A3})$$

## APPENDIX B: ANALYTIC EVOLUTION OF CARTESIAN P AND Q

The characteristic system of the Hamiltonian for of the Eikonal equation gives:

$$\frac{dp_i}{d\sigma} = \frac{1}{2} \frac{\partial}{\partial x_i}(V^{-2}), \quad \frac{dT}{d\sigma} = p_k p_k = V^{-2}. \quad (\text{B1})$$

From Eq. (B1) and because partial derivative  $\partial/\partial\gamma$  commutes with  $d/d\sigma$ , a simple *dynamic ray tracing system* can be derived as follows (subscript  $J$  for  $\gamma$  is omitted):

$$\frac{d}{d\sigma} Q_i^{(x)} = P_i^{(x)}, \quad \frac{d}{d\sigma} P_i^{(x)} = \frac{1}{2} \frac{\partial^2}{\partial x_i \partial x_j} (V^{-2}) Q_j^{(x)}. \quad (\text{B2})$$

For constant media gradient of  $V^{-2}$ , Eq. (B2) can be solved analytically for any point  $R$  at  $\sigma$  along the ray  $\Omega$  if  $\hat{\mathbf{Q}}^{(x)}$  and  $\hat{\mathbf{P}}^{(x)}$  are known at any other point  $S$  at  $\sigma_0$  along the ray  $\Omega$ :

$$\begin{aligned} P_{ij}^{(x)}(x_i) &= P_{ij}^{(x)}(S), \\ Q_{ij}^{(x)}(R) &= Q_{ij}^{(x)}(S) + (\sigma - \sigma_0) P_{ij}^{(x)}(S). \end{aligned} \quad (\text{B3})$$

### APPENDIX C: ANALYTIC EVOLUTION OF TRANSFORMATION MATRIX

For constant gradient of  $V^{-2}$ ,  $\hat{\mathbf{H}}$  can be solved analytically for any point  $R$  from any other point  $S$  along  $\Omega$ . This is achieved by computing the ray-centered coordinates unit basis  $\vec{e}_1$ ,  $\vec{e}_2$ , and  $\vec{e}_3$  that constitutes  $\hat{\mathbf{H}}$ , as  $\hat{H}_{ik} = \partial x_i / \partial q_k = \partial q_k / \partial x_i = e_{ki}$ ,  $i, k = 1, 2, 3, \dots$ . Consider a set of orthonormal unit vectors  $\vec{n}_1$ ,  $\vec{n}_2$ ,  $\vec{n}_3$  defined along ray  $\Omega$ , parameterized by  $\sigma$ . Let  $\vec{n}_3(\sigma) = V(\sigma) \vec{p}(\sigma)$  follow the tangent of the ray,  $\vec{n}_2(\sigma)$  is selected to be perpendicular to the ray plane,  $\vec{n}_1$  is then defined by  $\vec{n}_1 = \vec{n}_2 \times \vec{n}_3$ . Because the ray is a planar curve for constant gradient  $V^{-2}$ ,  $\vec{n}_2(\sigma) = \vec{n}_2(\sigma_0)$ . Given Eqs. (A1)–(A3),

$$\begin{aligned} \vec{n}_1(\sigma) &= \vec{n}_2(\sigma) \times \vec{n}_3(\sigma) = \vec{n}_2(\sigma) \times V(\sigma) \vec{p}(\sigma) \\ &= \vec{n}_2(\sigma_0) \times V(\sigma) \left( \vec{p}(\sigma_0) + \frac{1}{2} \vec{A}(\sigma - \sigma_0) \right). \end{aligned} \quad (\text{C1})$$

As  $\vec{e}_3$  coincides with  $\vec{n}_3$ ,  $\vec{e}_1(\sigma)$ ,  $\vec{e}_2(\sigma)$  can be determined from  $\vec{e}_1(\sigma_0)$ ,  $\vec{e}_2(\sigma_0)$  and the evolution of  $\vec{n}_1$ ,  $\vec{n}_2$  from  $\sigma_0$  to  $\sigma$  is

$$\begin{aligned} \vec{e}_1(\sigma) &= [\vec{e}_1(\sigma_0) \cdot \vec{n}_1(\sigma_0)] \vec{n}_1(\sigma) + [\vec{e}_1(\sigma_0) \cdot \vec{n}_2(\sigma_0)] \vec{n}_2(\sigma), \\ \vec{e}_2(\sigma) &= [\vec{e}_2(\sigma_0) \cdot \vec{n}_1(\sigma_0)] \vec{n}_1(\sigma) + [\vec{e}_2(\sigma_0) \cdot \vec{n}_2(\sigma_0)] \vec{n}_2(\sigma). \end{aligned} \quad (\text{C2})$$

### APPENDIX D: EVOLUTION OF RAY-CENTERED P AND Q

(1) Take initial condition for  $\mathbf{P}$ ,  $\mathbf{Q}$ . Assuming a point source  $S$  and  $\phi_0$  and  $i_0$  as the ray parameters  $\gamma_1$ ,  $\gamma_2$ :

$$\mathbf{Q}(S) = 0, \quad \mathbf{P}(S) = 1/V(S) \begin{pmatrix} 1 & 0 \\ 0 & \sin i_0 \end{pmatrix}.$$

- (2) Transform  $\mathbf{P}$ ,  $\mathbf{Q}$  into  $\hat{\mathbf{P}}^{(x)}$  and  $\hat{\mathbf{Q}}^{(x)}$  with  $\hat{H}$ ,  
(3) Analytically evolve  $\hat{\mathbf{P}}^{(x)}$  and  $\hat{\mathbf{Q}}^{(x)}$  by Eq. (B3),  
(4) Analytically evolve  $\hat{\mathbf{H}}$  by Eq. (C2),  
(5) Transform the evolved  $\hat{\mathbf{P}}^{(x)}$  and  $\hat{\mathbf{Q}}^{(x)}$  back to  $\mathbf{P}$ ,  $\mathbf{Q}$  with the evolved  $\hat{H}^T$ .

### APPENDIX E: CARTESIAN PARAXIAL TRAVEL TIME

For a field point  $R$ , and a point on the ray  $\gamma R_\gamma$  of the ray parameter  $\gamma_1$ ,  $\gamma_2$ , denote the Cartesian coordinates of  $R'$  and  $R_\gamma$  by  $x_i(R')$  and  $x_i(R_\gamma)$ , and  $x_i(R, R_\gamma) = x_i(R) - x_i(R_\gamma)$ , the quadratic expansion of  $T$  from  $T(R_\gamma)$  is

$$\begin{aligned} T(R, R_\gamma) &= T(R_\gamma) + x_i(R, R_\gamma) p_i^{(x)}(R_\gamma) \\ &\quad + \frac{1}{2} x_i(R, R_\gamma) x_j(R, R_\gamma) M_{ij}^{(x)}(R_\gamma), \end{aligned} \quad (\text{E1})$$

where  $M_{ij}$  are the elements of the  $3 \times 3$  matrix  $\hat{\mathbf{M}}^{(x)}$ :

$$\begin{aligned} \hat{\mathbf{M}}(R_\gamma) &= \hat{\mathbf{H}}(R_\gamma) \begin{pmatrix} \mathbf{M}(R_\gamma) & M_{13}(R_\gamma) \\ M_{13}(R_\gamma) & M_{23}(R_\gamma) \\ M_{13}(R_\gamma) & M_{23}(R_\gamma) & M_{33}(R_\gamma) \end{pmatrix} \\ &\quad \times \hat{\mathbf{H}}^T(R_\gamma). \end{aligned} \quad (\text{E2})$$

Here  $\mathbf{M}(R_\gamma)$  is defined in Eq. (2). The remaining elements can be derived<sup>7</sup> to be

$$\begin{aligned} M_{13}(R_\gamma) &= -(v^{-2} v_{,1})_{R_\gamma}, \quad M_{23}(R_\gamma) = -(v^{-2} v_{,2})_{R_\gamma}, \\ M_{33}(R_\gamma) &= -(v^{-2} v_{,3})_{R_\gamma}, \end{aligned} \quad (\text{E3})$$

$$\begin{aligned} v &= [V(q_1, q_2, s)]_{q_1=q_2=0, s=s(R_\gamma)}, \\ v_{,i} &= [\partial V(q_1, q_2, s) / \partial q_i]_{q_1=q_2=0, s=s(R_\gamma)}. \end{aligned} \quad (\text{E4})$$

$v_{,i}$  can be solved by transforming to Cartesian coordinates first:  $v_{,i} = \partial V / \partial q_i = H_{ki} \partial V / \partial x_k$ , and  $\partial V / \partial x_k$  can be solved analytically for constant gradient of  $V^{-2}$  by

$$\begin{aligned} \partial V^{-2} / \partial x_k &= -2V^{-3} \partial V / \partial x_k = A_k \Rightarrow \partial V / \partial x_k \\ &= -\frac{1}{2} V^3 A_k. \end{aligned} \quad (\text{E5})$$

### APPENDIX F: GAUSSIAN BEAM SUMMATION

The contributions of Gaussian beams are then summed up by integral superposition:

$$p(R, \omega) = \iint_{\mathcal{D}} \Phi(\gamma_1, \gamma_2) P^{\text{ray}}(R_\gamma) \exp[i\omega T(R, R_\gamma)] d\gamma_1 d\gamma_2. \quad (\text{F1})$$

The weighting function  $\Phi$  is derived to be

$$\begin{aligned} \Phi(\gamma_1, \gamma_2) &= (\omega/2\pi) [-\det(\mathbf{M}(R_\gamma) - \mathbf{M}^a(R_\gamma))]^{1/2} \\ &\quad \times |\det \mathbf{Q}^a(R_\gamma)| \end{aligned} \quad (\text{F2})$$

$$= (\omega/2\pi) [-\det(\mathbf{Q}^{aT}(\mathbf{M} - \mathbf{M}^a)\mathbf{Q}^a)]^{1/2}. \quad (\text{F3})$$

Matrices with suffix  $a$  ( $\mathbf{M}^a$ ,  $\mathbf{P}^a$ ,  $\mathbf{Q}^a$ ) represents the matrices of the *actual* ray field  $\Omega(\gamma_1, \gamma_2)$  [Eq. (2)]. They should be distinguished from the complex-valued  $\mathbf{M}$  used to describe the Gaussian beams [in Eq. (4)].

The choice of  $\text{Re}(\mathbf{M})$  is related to the curvatures of the wavefront and the choice of  $\text{Im}(\mathbf{M})$  is related to the width of the amplitude profile. They can be specified at  $R_\gamma$  or any other point along the central ray  $\gamma$  to control the shape of the beam. Techniques discussed in Ref. 51 are helpful for a good choice of  $\mathbf{M}$ .

<sup>1</sup>E. M. Salomons, *Computational Atmospheric Acoustics* (Springer Science & Business Media, New York, 2001), 335 pp.

<sup>2</sup>K. Attenborough, K. M. Li, and K. Horoshenkov, *Predicting Outdoor Sound* (CRC Press, Boca Raton, FL, 2006), 456 pp.

- <sup>3</sup>F. B. Jensen, W. A. Kuperman, M. B. Porter, and H. Schmidt, *Computational Ocean Acoustics* (Springer, New York, 2011), 794 pp.
- <sup>4</sup>A. D. Pierce, *Acoustics: An Introduction to Its Physical Principles and Applications* (McGraw-Hill, New York, 1981), pp. 371–423.
- <sup>5</sup>Q. Mo, H. Yeh, and D. Manocha, “Tracing analytic ray curves for light and sound propagation in non-linear media,” *IEEE Trans. Vis. Comput. Graphics* **22**(11), 2493–2506 (2016).
- <sup>6</sup>Q. Mo, H. Yeh, M. Lin, and D. Manocha, “Analytic ray curve tracing for outdoor sound propagation,” *Appl. Acoust.* **104**, 142–151 (2016).
- <sup>7</sup>V. Červený, *Seismic Ray Theory* (Cambridge University Press, Cambridge, UK, 2005), 722 pp.
- <sup>8</sup>K. Attenborough, S. Taherzadeh, H. E. Bass, X. Di, R. Raspet, G. R. Becker, A. Güdesen, A. Chrestman, G. A. Daigle, A. L’Espérance, Y. Gabillet, K. E. Gilbert, Y. L. Li, M. J. White, P. Naz, J. M. Noble, and H. A. J. M. van Hoof, “Benchmark cases for outdoor sound propagation models,” *J. Acoust. Soc. Am.* **97**(1), 173–191 (1995).
- <sup>9</sup>W. Luo and S. Henrik, “Three-dimensional propagation and scattering around a conical seamount,” *J. Acoust. Soc. Am.* **125**(1), 52–65 (2009).
- <sup>10</sup>L. R. Hole, “An experimental and theoretical study of propagation of acoustic pulses in a strongly refracting atmosphere,” *Appl. Acoust.* **53**(1), 77–94 (1998).
- <sup>11</sup>T. Van Renterghem, D. Botteldooren, and P. Lercher, “Comparison of measurements and predictions of sound propagation in a valley-slope configuration in an inhomogeneous atmosphere,” *J. Acoust. Soc. Am.* **121**(5), 2522–2533 (2007).
- <sup>12</sup>F. Sturm and A. Korakas, “Comparisons of laboratory scale measurements of three-dimensional acoustic propagation with solutions by a parabolic equation model,” *J. Acoust. Soc. Am.* **133**(1), 108–118 (2013).
- <sup>13</sup>M. S. Ballard, “Modeling three-dimensional propagation in a continental shelf environment,” *J. Acoust. Soc. Am.* **131**(3), 1969–1977 (2012).
- <sup>14</sup>V. E. Ostashev, D. K. Wilson, L. Liu, D. F. Aldridge, and N. P. Symons, “Equations for finite-difference, time-domain simulation of sound propagation in moving inhomogeneous media and numerical implementation,” *J. Acoust. Soc. Am.* **117**(2), 503–517 (2005).
- <sup>15</sup>D. K. Wilson and L. Liu, “Finite-difference, time-domain simulation of sound propagation in a dynamic atmosphere,” No. ERDC/CRREL-TR-04-12, Cold Regions Research and Engineering Lab, Hanover, NH (2004).
- <sup>16</sup>R. Blumrich and D. Heimann, “A linearized Eulerian sound propagation model for studies of complex meteorological effects,” *J. Acoust. Soc. Am.* **112**(2), 446–455 (2002).
- <sup>17</sup>Z. C. Zheng and W. Li, “Numerical stabilities and boundary conditions in time-domain Eulerian simulations of acoustic wave propagations with and without background flow,” *Appl. Math. Comp.* **202**(1), 146–161 (2008).
- <sup>18</sup>B. Cotté and P. Blanc-Benon, “Time-domain simulations of sound propagation in a stratified atmosphere over an impedance ground,” *J. Acoust. Soc. Am.* **125**(5), EL202–EL207 (2009).
- <sup>19</sup>D. Heimann and R. Karle, “A linearized Euler finite-difference time-domain sound propagation model with terrain-following coordinates,” *J. Acoust. Soc. Am.* **119**(6), 3813–3821 (2006).
- <sup>20</sup>B. de Greve, T. Van Renterghem, and D. Botteldooren, “Long range FDTD over undulating terrain,” in *Proceedings of Forum Acusticum* (2005), pp. 1141–1146.
- <sup>21</sup>D. Dagna, P. Blanc-Benon, and F. Poisson, “Time-domain solver in curvilinear coordinates for outdoor sound propagation over complex terrain,” *J. Acoust. Soc. Am.* **133**(6), 3751–3763 (2013).
- <sup>22</sup>T. Oshima, M. Imano, Y. Hiraguri, and Y. Kamoshida, “Linearized Euler simulations of sound propagation with wind effects over a reconstructed urban terrain using digital geographic information,” *Appl. Acoust.* **74**(12), 1354–1366 (2013).
- <sup>23</sup>D. G. Albert and L. Liu, “The effect of buildings on acoustic pulse propagation in an urban environment,” *J. Acoust. Soc. Am.* **127**(3), 1335–1346 (2010).
- <sup>24</sup>D. Dagna, P. Blanc-Benon, and F. Poisson, “Impulse propagation over a complex site: A comparison of experimental results and numerical predictions,” *J. Acoust. Soc. Am.* **135**(3), 1096–1105 (2014).
- <sup>25</sup>L. Liu and D. G. Albert, “Acoustic pulse propagation near a right-angle wall,” *J. Acoust. Soc. Am.* **119**(4), 2073–2083 (2006).
- <sup>26</sup>D. Heimann, “Wide-area assessment of topographical and meteorological effects on sound propagation by time-domain modeling,” *J. Acoust. Soc. Am.* **133**(5), EL419–EL425 (2013).
- <sup>27</sup>M. Hornikx, R. Waxler, and J. Forssén, “The extended Fourier pseudospectral time-domain method for atmospheric sound propagation,” *J. Acoust. Soc. Am.* **128**(4), 1632–1646 (2010).
- <sup>28</sup>M. Hornikx and R. Waxler, “The extended Fourier pseudospectral time-domain (PSTD) method for fluid media with discontinuous properties,” *J. Comp. Acoust.* **18**(04), 297–319 (2010).
- <sup>29</sup>J. Hofmann and K. Heutschi, “Simulation of outdoor sound propagation with a transmission line matrix method,” *Appl. Acoust.* **68**(2), 158–172 (2007).
- <sup>30</sup>G. Guillaume, P. Aumond, B. Gauvreau, and G. Dutilleul, “Application of the transmission line matrix method for outdoor sound propagation modelling Part 1: Model presentation and evaluation,” *Appl. Acoust.* **76**, 113–118 (2014).
- <sup>31</sup>P. Aumond, G. Guillaume, B. Gauvreau, C. Lac, V. Masson, and M. Bérengier, “Application of the transmission line matrix method for outdoor sound propagation modelling—Part 2: Experimental validation using meteorological data derived from the meso-scale model Meso-NH,” *Appl. Acoust.* **76**, 107–112 (2014).
- <sup>32</sup>T. Van Renterghem, E. M. Salomons, and D. Botteldooren, “Efficient FDTD-PE model for sound propagation in situations with complex obstacles and wind profiles,” *Acta Acust. Acust.* **91**(4), 671–679 (2005).
- <sup>33</sup>T. Van Renterghem, E. M. Salomons, and D. Botteldooren, “Parameter study of sound propagation between city canyons with a coupled FDTD-PE model,” *Appl. Acoust.* **67**(6), 487–510 (2006).
- <sup>34</sup>B. Bergen, B. Van Genechten, T. Van Renterghem, B. Pluymers, D. Vandepitte, D. Botteldooren, and W. Desmet, “Comparison of numerical prediction techniques for sound propagation in complex outdoor environments,” in *15th International Congress on Sound and Vibration* (2008).
- <sup>35</sup>H. Yeh, R. Mehra, Z. Ren, L. Antani, D. Manocha, and M. C. Lin, “Wave-ray coupling for interactive sound propagation in large complex scenes,” *ACM Trans. Graph.* **32**(6), 165 (2013).
- <sup>36</sup>N. Raghuvanshi, R. Narain, and M. C. Lin, “Efficient and accurate sound propagation using adaptive rectangular decomposition,” *IEEE Trans. Vis. Comput. Graphics* **15**(5), 789–801 (2009).
- <sup>37</sup>R. Mehra, N. Raghuvanshi, A. Chandak, D. G. Albert, D. K. Wilson, and D. Manocha, “Acoustic pulse propagation in an urban environment using a three-dimensional numerical simulation,” *J. Acoust. Soc. Am.* **135**(6), 3231–3242 (2014).
- <sup>38</sup>H. Kuttruff, *Room Acoustics* (CRC Press, Boca Raton, FL, 2009), 392 pp.
- <sup>39</sup>J. B. Allen and D. A. Berkley, “Image method for efficiently simulating small-room acoustics,” *J. Acoust. Soc. Am.* **65**(4), 943–950 (1979).
- <sup>40</sup>J. Borish, “Extension of the image model to arbitrary polyhedra,” *J. Acoust. Soc. Am.* **75**(6), 1827–1836 (1984).
- <sup>41</sup>M. Vorländer, “Simulation of the transient and steady-state sound propagation in rooms using a new combined ray-tracing/image-source algorithm,” *J. Acoust. Soc. Am.* **86**(1), 172–178 (1989).
- <sup>42</sup>M. Taylor, A. Chandak, Q. Mo, C. Lauterbach, C. Schissler, and D. Manocha, “Guided multiview ray tracing for fast auralization,” *IEEE Trans. Vis. Comput. Graphics* **18**(11), 1797–1810 (2012).
- <sup>43</sup>T. Funkhouser, I. Carlbom, G. Elko, G. Pingali, M. Sondhi, and J. West, “A beam tracing approach to acoustic modeling for interactive virtual environments,” in *Proc. of the 25th Conf. on Comp. Graph. and Interactive Tech.* (1998).
- <sup>44</sup>C. Schissler, R. Mehra, and D. Manocha, “High-order diffraction and diffuse reflections for interactive sound propagation in large environments,” *ACM Trans. Graph.* **32**(4), 39 (2014).
- <sup>45</sup>P. A. Baxley, H. Buckler, and M. B. Porter, “Comparison of beam tracing algorithms,” in *Proc. of the 5th European Conference on Underwater Acoustics* (2000).
- <sup>46</sup>Y. Gabillet, H. Schroeder, G. A. Daigle, and A. L’Espérance, “Application of the Gaussian beam approach to sound propagation in the atmosphere: Theory and experiments,” *J. Acoust. Soc. Am.* **93**(6), 3105–3116 (1993).
- <sup>47</sup>K. M. Li, S. Taherzadeh, and K. Attenborough, “An improved ray-tracing algorithm for predicting sound propagation outdoors,” *J. Acoust. Soc. Am.* **104**(4), 2077–2083 (1998).
- <sup>48</sup>J. M. Prospathopoulos and S. G. Voutsinas, “Determination of equivalent sound speed profiles for ray tracing in near-ground sound propagation,” *J. Acoust. Soc. Am.* **122**(3), 1391–1403 (2007).
- <sup>49</sup>J. M. Klosner, L. B. Felsen, I. T. Lu, and H. Grossfeld, “Three-dimensional source field modeling by self-consistent Gaussian beam superposition,” *J. Acoust. Soc. Am.* **91**(4), 1809–1822 (1992).
- <sup>50</sup>T. Heilpern, E. Heyman, and V. Timchenko, “A beam summation algorithm for wave radiation and guidance in stratified media,” *J. Acoust. Soc. Am.* **121**(4), 1856–1864 (2007).
- <sup>51</sup>E. Svensson, “Gaussian beam summation in shallow waveguides,” *Wave Motion* **45**(4), 445–456 (2008).